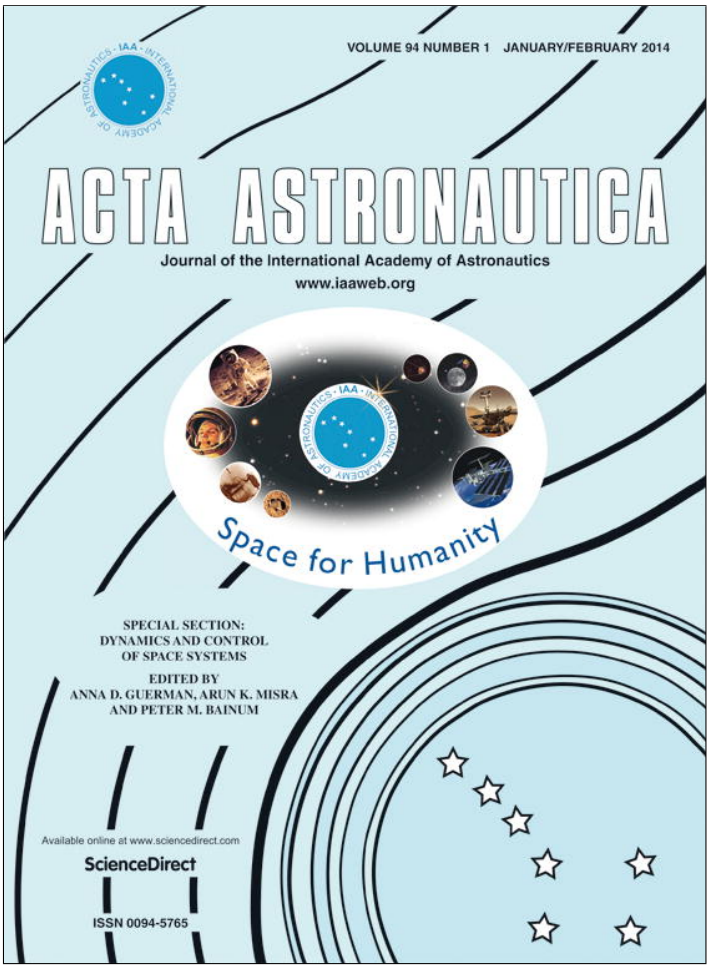

Acta Astronautica 94 (2014) 502–514

Contents lists available at ScienceDirect

Acta Astronautica

journal homepage: www.elsevier.com/locate/actaastro

Stability of spinning satellite under axial thrust and internal mass motion

Frank L. Janssens [a], Jozef C. van der Ha [b,*]

[a] Wilhelminastraat 29, 2201 KA Noordwijk, The Netherlands
[b] 5808 Bell Creek Road, Deming, WA 98244, USA

ARTICLE INFO

Article history:
Received 11 June 2012
Received in revised form
15 September 2012
Accepted 18 September 2012
Available online 30 November 2012

Keywords:
Attitude dynamics
Axial thrust
Internal motion
Stability
STAR-48

ABSTRACT

This paper considers a spinning rigid body and a particle with internal motion under axial thrust. This model is helpful for gaining insights into the nutation anomalies that occurred near the end of orbit injections performed by STAR-48 rocket motors. The stability of this system is investigated by means of linearized equations about a uniform spin reference state. In this model, a double root does not necessarily imply instability. The resulting stability condition defines a manifold in the parameter space. A detailed study of this manifold and the parameter space shows that the envelope of the constant solutions is in fact the stability boundary. Only part of the manifold defines a physical system and the range of frequency values that make the system unstable is restricted. Also it turns out that an increase of the spring stiffness, which restrains the internal motion, does not necessarily increase the stability margin. The application of the model is demonstrated using the orbit injection data of ESA's Ulysses satellite in 1990.

1. Introduction

After decades of successful upper stage firings using spinning solid rocket motors, the fast growth rates of the nutation angle that occurred toward the end of STAR-48 burns, came as a total surprise. Flandro et al. [1] provides a list of twelve PAM-D[1] orbit injections, of which nine showed an excessive nutation angle at the end of the burn. The STAR-48 was the engine commonly used in the 1980s as integrated in the Perigee Assist Motor module (PAM). A novel feature of the STAR-48 was that, in an attempt to shorten the engine length, the nozzle was made partially re-entrant in the combustion chamber. This design change introduced somehow, depending on the PAM/spacecraft configuration, an instability mechanism at the end of the burn.

This attitude instability inspired many investigations, see Refs. [1–18]. Eventually, it became clear that only two research directions were promising. The first pointed to instability of the gas dynamics within the combustion chamber due to the fact that the new complex shape of the burning surface changed the gas flow significantly. The second mechanism is known as the 'slag model'. It studies the internal motion of the combustion products (i.e., Al_2O_3 particles) that may accumulate as liquid slag within the collar of the STAR-48 re-entrant nozzle. A prospective explanation must involve a sufficiently large transverse torque to overcome the jet damping effect (see Ref. [19]) near the end of the burn. Gradually, a preference for the slag model mechanism emerged as the main cause of instability with a possible contribution of the internal gas flow.

A full description of the nutation problem should start from a set of non-linear time-varying equations coupled

* Corresponding author.
E-mail addresses: fjanssens@ziggo.nl (F.L. Janssens), jvdha@aol.com (J.C. van der Ha).

[1] PAM refers to the 'Perigee Assist Motor' upper stage. PAM-D is the stage that includes the STAR-48 solid motor which is the most frequently used perigee kick motor for geosynchronous injections; for Ulysses, the PAM-S was used.

0094-5765/$ - see front matter © 2012 IAA. Published by Elsevier Ltd. All rights reserved.
http://dx.doi.org/10.1016/j.actaastro.2012.09.013

to the three-dimensional gas flow equations but its complexity would be overwhelming. A practical approach is to study somewhat restricted models that may explain some aspects of the observed instability. As a first step, it should be verified that a misaligned thrust or a realistic time-varying thrust profile cannot cause the instability. This issue is studied in Ref. [2].

Refs. [1,3,4] provide examples of gas dynamic studies. Flandro et al. [1] summarize the effects of an un-steady vortex flow by transverse torque components that are proportional to the transverse rates. His full model may indeed generate instability but is very sensitive to the system parameters and initial conditions. Meyer [3] starts by expanding classical flow results to include the entering (combustion front) and exit of the gases through the nozzle. Misterek et al. [4] perform numerical simulations on two two-dimensional steady-flow problems but obtains only stabilizing torques.

Janssens [5] uses Flandro's summarizing model [1] in a time-varying version. The expressions for the nutation frequency and jet damping take account of the variations of the mass and moments of inertia during the burn. The results give a higher nutation frequency and a reduced jet damping torque which agrees with the flight data. However, in order to overcome the jet damping, the instability needs to start at the beginning of the burn, which is not compatible with the flight data. Meyer [6] performs different gas dynamic studies and concludes that the gas dynamics effects may only provide a minor contribution to the observed instability. Unfortunately, none of the global investigations is capable of establishing good agreements with *all* available flight data.

The liquid-slag hypothesis has been proposed by Mingori, Or, et al. (see Refs. [7–11]). The main objective was to acquire better insights into the instability mechanism by studying the linearized equations that include the thrust and internal particle motion. These models use the constant mass properties at the end of the burn. For the internal particle motion several models have been proposed. In this paper the model of Refs. [7–9] is used where the particle may move in a plane perpendicular to the spin axis to which it is attached by a spring. This model indeed produces a coning instability due to the coupling of the nutation with a particle located aft of the system center of mass.

Other internal-motion models that may produce instability are a spherical pendulum or two pendulums in a meridian plane (see Refs. [10,11]). Cochran and Kang [12–14] simulate the non-linear dynamics of a body augmented with a spherical pendulum and show that parametric resonances are possible. However, Refs. [12–14] do not present compelling evidence that such resonances are compatible with the observed nutation instability. When modeling the internal motion by a pendulum, we only need its length and mass for which a range of realistic values is available. The instability should occur within this range of parameters which is in fact not the case in Ref. [10].

The physical meaning of the restoring force that counteracts the centrifugal force in the elastic spring model is not at all clear. Here, we interpret the spring stiffness as a 'tuning' parameter for matching the flight data. The introduction of a spring may be avoided by using the constraint force to keep the liquid slag in contact with either the nozzle collar or the combustion chamber wall depending on the spin-to-thrust ratio, see Meyer [6].

At the time in the 1980s when the nutation instabilities occurred, little was known about the amount of slag that may accumulate during a solid rocket burn of about 85 s. In fact, at the time of the Ulysses launch in 1990, the estimates for the STAR-48 varied from 10 kg to over 100 kg. As expected, also this topic generated lots of research (see, for instance, Ref. [15]). In 2000, Ref. [16] provides a list of 53 research papers on the most likely values of the slag masses. The current estimates start at 4 kg whereas Or and Challoner [11] use 9 and 27 kg in their work.

In a pioneering paper, Mingori and Yam [7] obtain a stability condition for their model in terms of two non-dimensional parameters, i.e. β^2 and T_0, which comprise all of the eight physical parameters of their model. This stability condition describes a manifold in the eight-dimensional parameter space. In this paper we clarify and interpret the meaning of this stability boundary in terms of the parameters (i.e., mass and spring stiffness) that define the particle's internal motion.

The next section introduces the nomenclature of the parameter space. The dependencies of the derived parameters on the particle and spring (which cause the instability) are separated, as far as possible, from the remaining six physical parameters. Subsequently, we rewrite the equations of motion from Ref. [7] in terms of the independent parameters of the body and particle components and not in the system parameters. Next, we treat two special cases, i.e. zero stiffness and the particle at the body Center of Mass (CoM), to obtain better insights in the dynamics. The results illustrate the complex relationship between the stability boundary and the physical parameters.

Subsequently, we establish the condition for the existence of constant (or stationary) solutions. This generates a family of linear equations $T_0(\beta^2)$. A new insight is that the envelope of these lines with respect to the inertia ratio produces the stability boundary. Afterwards, we derive the stability boundary by using complex variables and clarify the physical meaning of this transformation. We find the stability condition as an implicit function of the same two non-dimensional parameters $\{\beta^2, T_0\}$ as in Ref. [7] and not as a set of coupled equations. Next, we express the stability boundary in terms of the normalized particle mass and spring stiffness. The result shows that only part of the stability condition, as expressed in β^2 and T_0, corresponds to a physical system. Finally, we derive boundaries for the values of the double root on the stability boundary.

2. Model data and nomenclature

2.1. Physical model

Fig. 1 shows the physical model studied here which is identical to the one used in Refs. [7,8]. It consists of a symmetric rigid body of constant mass M and principal moments of inertia C (axial) and A_b (transverse). The body

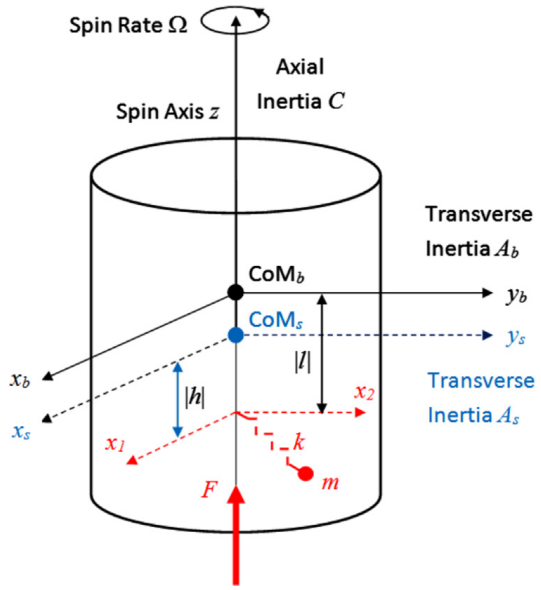

Fig. 1. Reference configuration for model.

Table 1
Summary of physical parameters.

Parameter	Unit	Description
M	kg	Body mass
C	kg m^2	Axial moment of inertia (spin inertia)
A_b	kg m^2	Transverse moment of inertia for axes passing through body CoM
F	N	Thrust level of rocket motor
Ω	rad/s	Spin rate
l	m	Vertical coordinate of particle relative to body CoM
m	kg	Particle mass
k	kg/s^2	Spring constant or stiffness

includes the mass properties of the spacecraft, the STAR-48 solid motor casing, and remaining PAM hardware at the end of the burn. It spins at constant spin rate Ω and is subjected to a thrust F which is assumed to be perfectly pointing along the spin axis.

The particle of mass m is introduced to generate a potential instability mechanism through internal motion. It represents the accumulated slag or a feature of the gas flow of a motor with a re-entrant nozzle. The particle is nominally located on the spin axis at distance l from the body center of mass. For $l>0$, the particle is on the $+z$ axis and for $l<0$ it is on the $-z$ axis. The particle may move in an equatorial plane while attached to the spin axis by a linear spring of stiffness k.

The point of application of the thrust is also taken at the distance l from the center of mass even though it is usually taken within the nozzle exit plane. This assumption is acceptable for a motor with a re-entrant nozzle and avoids the introduction of yet another independent parameter.

Table 1 summarizes the eight independent parameters of our model. For a given spacecraft/PAM configuration, all of the inputs M, C, A_b, F, and l are essentially frozen. The final two parameters m and k will play a different role in the discussion of the results. Ref. [10] gives a similar list for the case when the internal motion is modeled by a spherical pendulum. (The pendulum attachment distance and the pendulum length are the parameters replacing k and m).

2.2. Derived and auxiliary parameters

Table 2 summarizes the derived and auxiliary parameters. The first three rows provide the system parameters. The total mass of the system is $M+m$ and the associated mass ratio is μ. The presence of the slag mass m changes the lever arm of the particle to the system CoM$_s$ from l to h.

Although the difference between h and l is small when $m \ll M$, we prefer to use l since it is independent of m. The spin inertia C remains unchanged when the particle is on the spin axis but changes by the amount mr^2 when the particle is at a distance r from the spin axis. This second-order term drops out when the equations are being linearized in terms of r. Refs. [7–9] employ the transverse system inertia $A_s=I_1+mh^2$ where I_1 is the transverse inertia of the body alone but relative to the system CoM$_s$. Therefore, I_1 has a hidden dependency on m due to the shift from CoM$_b$ to CoM$_s$ which introduces a transfer term in the transverse inertia moment.

The following eight rows in Table 2 define the non-dimensional parameters that help reducing the complexity of the equations. The angle τ replaces t as independent variable. The inertia ratio $\lambda=C/A_b$ is equal to the symbol Λ in Refs. [7–9] but its meaning is not transparent. For a satellite with an appended solid motor, the spin axis is the minimum axis of inertia, i.e. $\lambda<1$, but all results remain valid for $\lambda>1$ as well.

The normalized spring constant k_n is defined in terms of $p_k=A_b\Omega^2/l^2$, which is independent of k and m. The thrust F is normalized by $p_{th}=A_b\Omega^2/|l|$ where the absolute value of the particle's axial position keeps p_{th} positive. For stability, it turns out that $l<0$ is the more interesting case. The mass-spring resonance frequency has been normalized by the square of the spin rate and helps in interpreting the results. We analyze the stability conditions in terms of k_n and μ for a system defined by the normalization parameters p_k, p_{th}, p_{res}, f, and λ.

Finally, the last two rows of Table 2 provide the definitions of the non-dimensional parameters $\{\beta^2,T_0\}$. They are useful because the stability diagram may be expressed by a single curve $T_0(\beta^2)$ which is valid for all possible physical systems (see Refs. [7–9]). A single point $\{\beta^2,T_0\}$ provides only one relationship between the eight independent parameters and represents many physical systems. The definitions in Table 2 show that T_0 depends on the difference between k and m whereas β^2 represents the ratio k/m. This distinction is less transparent in the formulations of Refs. [7–9].

The parameters in Table 2 are well suited for studying the general case, i.e. in the absence of singularities. For special cases such as zero stiffness k or zero length l, different parameter combinations may be more efficient and will be used as appropriate. For example, if the spring constant k vanishes, we have the point $\{\beta=0, T_0=-\mu f/\lambda^2\}$

Table 2
Summary of auxiliary parameters.

Parameter	Unit	Definition	Description
μ	–	$m/(M+m)$; $1-\mu=M/(M+m)$	Ratio relationship between particle and total mass
h	m	$(1\text{-}\mu)l$	Vertical distance of particle to the system CoM_s
A_s	kg m^2	$A_b+(1-\mu)ml^2$	Transverse moment of inertia relative to system CoM_s
τ	–	Ωt	Angular independent variable
$0<\lambda<2$	–	C/A_b	Precession rate of angular velocity, normalized by the spin rate Ω; $\lambda-1$ is the nutation rate with $\lambda-1<0$ if $C<A_b$
$p_k>0$	kg/s^2	$A_b\Omega^2/l^2$	Auxiliary parameter
$k_n\geq 0$	–	k/p_k	Normalized spring constant or stiffness
$p_{th}>0$	kg m/s^2	$A_b\Omega^2/\|l\|$	Auxiliary parameter
f	–	F/p_{th}	Normalized thrust force of rocket motor
$p_{res}>0$	–	$A_b/(Ml^2)$	Auxiliary parameter
ω_{res}^2	–	$k/(m\,\Omega^2)$	Normalized resonance frequency of m attached to a fixed point (with an elastic spring of stiffness k)
β_λ^2, β^2	–	$\beta_\lambda^2=\omega_{res}^2/(1-\mu)$; $\beta^2=\beta_\lambda^2/\lambda^2$	$\Rightarrow \beta_\lambda^2=p_{res}k_n/\mu$
$T_{0\lambda}$, T_0	–	$T_{0\lambda}=k_n-\mu f$; $T_0=T_{0\lambda}/\lambda^2$	$\Rightarrow T_{0\lambda}=(k\,l^2-\mu\|l\|F)/A_b\Omega^2$

Table 3
Summary of Ulysses derived parameters (at end of burn).

Parameter	Unit	Value
λ	–	0.67085
$p_{res}>0$	–	0.42659
$p_k>0$	kg/s^2	14225
$p_{th}>0$	N	21337
f	–	3.3744
$(\beta_\lambda^2)_{max}=fp_{res}$	–	1.4395
$\beta_\lambda^2=\beta^2\lambda^2$	–	$0.42659k_n/\mu$
$T_{\lambda 0}=\lambda^2T_0$	–	$k_n-3.3744\mu$
m_{lim} (for $k=0$)	kg	20.232

which is a perfectly valid physical system. Table 2 shows that the condition $T_0=0$ may occur in two ways, i.e. either due to $l=0$ when the particle is attached in the plane of the body CoM_b, irrespective of any other parameters, or when $k_n=\mu f$. An interpretation of the latter condition is provided in the next section. We also use the parameters β_λ^2 and $T_{0\lambda}$ in order to separate the dependency on the inertia ratio λ.

With the definitions in Table 2, the stability boundary consists of a family of curves parameterized in λ. In practice, we study the influence of $\{k, m\}$ on the stability of the system given by:

$$\beta^2=f_\beta(k,m;M,A_b,C,\Omega);\ T_0=f_T(k,m;M,A_b,C,\Omega;F,l)$$

The numerical example uses the data of the Ulysses injection into a trajectory to Jupiter by the Shuttle Discovery in December 1990 by a special PAM-S version that contains the STAR-48 motor (see Refs. [17,18]). The mass properties at the end of the burn are $M=365.16$ (Ulysses)+221.4 (dry mass PAM-S)=586.56 kg; $C=301.43$ (Ulysses)+76.26 (PAM-S)=377.69 kgm^2; $A_b=563$ kgm^2 (i.e., the average value of the transverse inertias as Ulysses is asymmetric due to the presence of an RTG); $l=-1.5$ m; $\Omega=72$ rpm; $F=72$ kN. The final acceleration is about $12g$ which is much larger than for any previous injection by a PAM module. These data were essentially frozen before the launch. Table 3 summarizes the main derived parameters for Ulysses.

3. Results for the transverse dynamics

3.1. Equations of motion

The model to be analyzed here consists of an axi-symmetric spinning rigid body augmented with a mass particle that may move within a plane normal to the spin axis. The reference motion consists of a body spinning at a constant rate Ω and the particle located on the spin axis. The linearized equations of the transverse dynamics about this reference motion are described by the first-order variables $\{\omega_1, \omega_2, x_1, x_2\}$. The rates ω_1, ω_2 are the transverse angular velocity components, normalized by the spin rate Ω, in a body-fixed reference frame. The variables x_1, x_2 are the components of the particle displacement relative to the spin axis, see Fig. 1.

Refs. [7–9] provide the relevant equations of motion within a principal reference frame with origin at the system CoM_s. We modify these equations by using the nomenclature defined in Table 2 and adopt τ as the independent variable with $(\cdot)'$ denoting $d(\cdot)/d\tau$. This leads to the following system of equations:

$$A_s\omega_1'+(C-A_s)\omega_2=mh\{x_2''+2x_1'-x_2\}-(\mu F/\Omega^2)x_2$$

$$A_s\omega_2'-(C-A_s)\omega_1=mh\{-x_1''+2x_2'+x_1\}+(\mu F/\Omega^2)x_1$$

$$x_1''-2x_2'-\{1-\omega_{res}^2/(1-\mu)\}x_1=-h(\omega_2'+\omega_1)/(1-\mu)$$

$$x_2''+2x_1'-\{1-\omega_{res}^2/(1-\mu)\}x_2=h(\omega_1'-\omega_2)/(1-\mu) \qquad (1a-d)$$

Eqs. (1a,b) are the standard Euler equations with torques due to the thrust force and the particle's motion. Eqs. (1c,d) describe the internal motion of the particle which may be excited by the transverse rates ω_1, ω_2

Next, we eliminate the terms within $\{\ldots\}$ on the right-hand-sides of Eqs. (1a,b) by using Eqs. (1d,c), respectively. Furthermore, we write Eqs. (1a,b) in terms of the moments of inertia relative to the body CoM_b:

$$A_b\omega_1'+(C-A_b)\omega_2+\{ml\omega_{res}^2+\mu F/\Omega^2\}x_2=0$$

$$A_b\omega_2'-(C-A_b)\omega_1-\{ml\omega_{res}^2+\mu F/\Omega^2\}x_1=0 \qquad (2a,b)$$

The identical terms within {…} in Eqs. (2a,b) may be expressed in terms of the parameter $T_{0\lambda}$ defined in the last row of Table 2 as follows:

$$\{ml\omega_{res}^2+\mu F/\Omega^2\}=A_b(k_n-\mu f)/l=A_bT_{0\lambda}/l \tag{3}$$

The negative sign in front of f holds for a particle located aft of the CoM_b for which $l<0$.

Subsequently, the terms on the right-hand-sides of Eqs. (1c,d) can be simplified by means of Eqs. (2) and (3):

$$l(\omega_2'+\omega_1)=l\lambda\omega_1+(k_n-\mu f)x_1=l\lambda\omega_1+T_{0\lambda}x_1$$

$$l(\omega_1'-\omega_2)=-l\lambda\omega_2-(k_n-\mu f)x_2=-l\lambda\omega_2-T_{0\lambda}x_2 \tag{4a, b}$$

The final form of the system of Eqs. (1) becomes:

$$\omega_1'+(\lambda-1)\omega_2+T_{0\lambda}x_2/l=0$$

$$\omega_2'-(\lambda-1)\omega_1-T_{0\lambda}x_1/l=0$$

$$x_1''-2x_2'-(1-\beta_\lambda^2-T_{0\lambda})x_1+l\lambda\omega_1=0$$

$$x_2''+2x_1'-(1-\beta_\lambda^2-T_{0\lambda})x_2+l\lambda\omega_2=0 \tag{5a – d}$$

The transition from Eqs. (1) to (5) corresponds to a shift in the origin from the *system* CoM_s to the *body* CoM_b. (Note that the angular velocity is independent of the reference point on the body). The combined parameters β_λ^2 and $T_{0\lambda}$ show up naturally in this formulation. Eqs. (5) may also be obtained directly by the Newton–Euler method as was done in Ref. [10]. The two approaches are equivalent.

Eqs. (5) have accomplished the separation of the derivative terms of the ω_i and x_i ($i=1, 2$) variables. Furthermore, the parameters appearing in Eqs. (5) refer exclusively to the body and the particle's position within the body. The terms $x_i''\pm 2x_k'-x_i$ (for $i,k=1,2$) in Eqs. (5c,d) describe the relative motion of a particle on a spinning base. The remaining force terms in Eqs. (5c,d) are due to the spring, the thrust, and the nutation of the body, respectively.

The 6-th order system in Eqs. (5) is suitable for stability analyses but contains no information on the orientation of the body. The orientation can be obtained by introducing two supplementary equations for the small attitude angles $\{\theta_1,\theta_2\}$ in terms of the rates ω_i ($i=1, 2$). The corresponding 8-dimensional system of equations is given in Appendix A in matrix form.

Fig. 2 illustrates the two torques acting on the body for the special case when $x_1=0$ and $x_2>0$. Eq. (5a) shows that the total normalized torque is $-T_{0\lambda}x_2/l$. The physical torque T in Fig. 2 has two components acting along the x_1-axis:

$$T=kx_2|l|-\mu x_2F=(A_b\Omega^2)T_{0\lambda}x_2/|l|$$

The torque due to the spring is positive and the torque due to the thrust is negative and is identical to the thrust torque about CoM_s. The sign of $T_{0\lambda}$ determines whether the result is repelling or attracting.

3.2. Special solutions for $T_0=0$

The case $T_0=0$ occurs when either $l=0$ or $k_n=\mu f$ as seen from Table 2 and subsequent text. In the first case we have $h=l=0$ and $A_s=A_b$ with the consequence that the three normalization constants p_k, p_{th}, and p_{res} are singular.

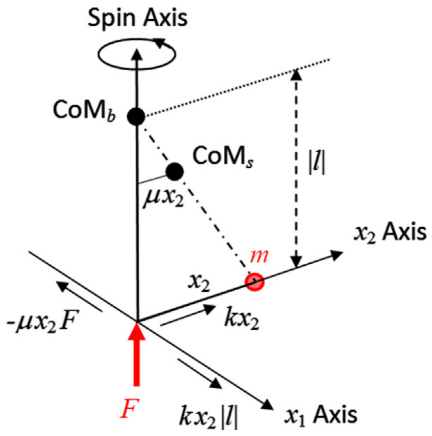

Fig. 2. Illustration of torques acting on the body.

Nevertheless, the $T_{0\lambda}/l$ terms in Eqs. (5a,b) remain well defined when $l\to 0$. This can be confirmed with the help of the definition of $T_{0\lambda}$ in Table 2:

$$lim_{l\to 0}\{T_{0\lambda}/l\}=lim_{l\to 0}\{lk+\mu F\}/(A_b\Omega^2)=\mu F/(A_b\Omega^2) \tag{6}$$

Therefore, in the special case $l=0$, the system in Eqs. (5) takes the following form:

$$\omega_1'+(\lambda-1)\omega_2+\mu Fx_2/\left(A_b\Omega^2\right)=0$$

$$\omega_2'-(\lambda-1)\omega_1-\mu Fx_1/\left(A_b\Omega^2\right)=0$$

$$x_1''-2x_2'-(1-\beta_\lambda^2)x_1=0$$

$$x_2''+2x_1'-(1-\beta_\lambda^2)x_2=0 \tag{7a – d}$$

The characteristic equation of the system in Eqs. (7) factors into two decoupled parts:

$$p^2+(\lambda-1)^2=0;\quad p^4+2(1+\beta_\lambda^2)p^2+(1-\beta_\lambda^2)^2=0 \tag{8a, b}$$

Eq. (8a) produces the two roots $p_{1,2}=\pm j(\lambda-1)$ which correspond to the body's nutation. The particle does not participate in this motion and remains at its initial axial position. The eigenvectors corresponding to these roots are $[\omega_1,\ \pm j\omega_1,\ 0,\ 0]^T$, respectively.

The four roots of the bi-quadratic equation in Eq. (8b) can be calculated as

$$p_{3,4}=\pm j(1+\lambda\beta);\quad p_{5,6}=\pm j(1-\lambda\beta) \tag{9a, b}$$

In the case when $l=0$, β_λ^2 has positive values and the roots in Eqs. (9) remain on the imaginary axis. The results in Eqs. (9) indicate that the motion is marginally (or oscillatory) stable as long as $\beta_\lambda\neq 1$. In these modes, the circular particle motion x_1, x_2 goes together with a similar motion in the rates ω_1, ω_2. In the case when $l\neq 0$, the condition $T_0=0$ implies that β_λ^2 can assume only one possible value, i.e. $\beta_\lambda^2=fp_{res}$, see Table 2. If the value of fp_{res} happens to be equal to 1 (i.e., when $\omega_{res}^2=1-\mu$), then $\beta_\lambda=1$ and $p_{5,6}$ is a double zero root for $l=0$ as well as for $l\neq 0$. In the section "Constant solutions" we will show in detail that also these solutions are marginally stable.

3.3. Special solutions for $k=0$ ($\beta^2=0$)

In this case, the restoring force on the particle is zero. Because of the gyroscopic coupling effect between the

particle and the rotating body, the case $k=0$ is not necessarily meaningless or even unstable. In fact, it defines an end point on the stability curve. In order to simplify Eqs. (5) for the special case $k=0$ we introduce the parameter l_r based on the definition of $T_{0\lambda}$ in Table 2:

$$(T_{0\lambda})_{k=0}=\frac{\mu F l}{A_b\Omega^2}=\frac{\mu f l}{|l|}=\frac{l}{l_r}\ \text{with}:\ l_r=\frac{|l|}{\mu f} \tag{10a, b}$$

Eqs. (5) can now be reduced to the following form:

$$\begin{aligned}&\omega_1'+(\lambda-1)\omega_2+x_2/l_r=0\\&\omega_2'-(\lambda-1)\omega_1-x_1/l_r=0\\&x_1''-2x_2'-(1-l/l_r)x_1+l\lambda\omega_1=0\\&x_2''+2x_1'-(1-l/l_r)x_2+l\lambda\omega_2=0\end{aligned} \tag{11a – d}$$

and the corresponding 6-th order characteristic equation can be written as

$$(p^2+1)\{(p^2+l/l_r+\lambda-1)^2+p^2(\lambda-2)^2\}=0 \tag{12}$$

The roots $p_{1,2}=\pm j$ are associated with the spin frequency and they are always a solution (for any value of m). The eigenvectors corresponding to the spin frequency are as follows:

$$[j/(\lambda l_r),-1/(\lambda l_r),-j,1]^T \tag{13}$$

This shows that the particle is always located opposite of the transverse angular velocity vector.

The second part of Eq. (12) is a bi-quadratic equation for the remaining four roots:

$$\begin{aligned}p_{3,4}&=j(1-\lambda/2\pm\sqrt{l/l_r+\lambda^2/4})\\p_{5,6}&=j(-1+\lambda/2\pm\sqrt{l/l_r+\lambda^2/4})\end{aligned} \tag{14a, b}$$

As long as the expression under the square root is positive, these roots are on the imaginary axis and the system is oscillatory stable. The expression under the square root can only become zero (and negative) if l is negative because the other two parameters l_r and λ^2 are always positive. This means that the particle must be aft of the body CoM$_b$.

In the case when the term under the square root in Eqs. (14) is negative the system is unstable. Thus, the imaginary part $\lambda/2-1$ of the roots p_i ($i=3,\ldots,6$) is the limiting value where the roots leave the imaginary axis and start obtaining opposite real parts. For a satellite body, the value of $\lambda/2-1$ is always non-zero (note that$\lambda=2$ for a flat plate).

Fig. 3 shows the evolution of the roots p_3 and p_4 as functions of m. The starting positions on the imaginary axis correspond to $m=\mu=0$ which implies that $l/l_r=(T_{0\lambda})_{k=0}=0$, see Eq. (10a). Eq. (14a) shows that $p_3=j$ and $p_4=j(1-\lambda)$, i.e. the spin and nutation frequencies of the body, respectively. For increasing values of m, the two roots approach each other and become equal to $1-\lambda/2$ when $l/l_r=-\lambda^2/4$ or $T_0=-1/4$. The particle mass ratio at this point follows from Eq. (10a):

$$(T_0)_{k=0,\lim}=\mu_{lim}\frac{F l}{A_b\lambda^2\Omega^2}=-\frac{1}{4}\Rightarrow\mu_{lim}=\frac{1}{4}\frac{C^2\Omega^2}{A_b|l|F} \tag{15a, b}$$

When the parameters M, F, C, and A_b are known, Eq. (15b) provides the relationship between the limiting permissible slag mass m_{lim} and the spin rate Ω as follows:

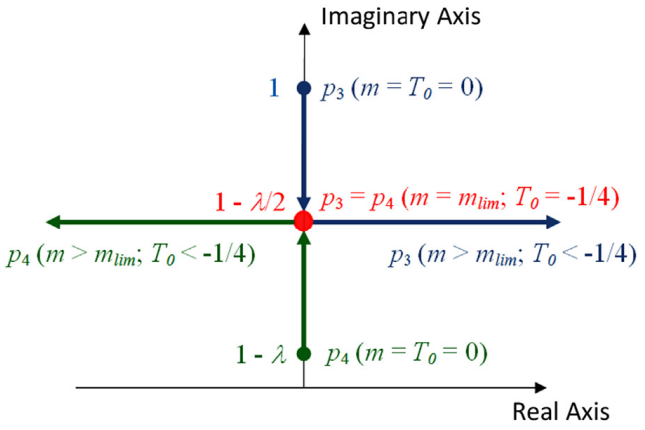

Fig. 3. Evolution of roots p_3 and p_4 as functions of m.

$$m_{lim}=M\frac{\Omega^2}{\Omega_M^2-\Omega^2},\quad\text{with}:\ \Omega_M=\frac{2}{C}\sqrt{A_b|l|F} \tag{16a, b}$$

For further increasing mass values beyond m_{lim}, the two roots leave the imaginary axis in opposite directions (see Fig. 3) and the resulting motion becomes unstable.

The stability condition in Eqs. (15) may also be expressed as a condition on the distance $|l|$:

$$|l|\ \le\ \frac{1}{4}\frac{C^2\Omega^2}{A_bF}\left(1+\frac{M}{m}\right) \tag{17}$$

This expression agrees with results in Refs. [7–9]. Furthermore, it has been derived in Ref. [18] and is cited in Ref. [22]. An interesting interpretation of Eq. (17) is that there is a limit on the distance that the particle may be aft of the body CoM$_b$ for a given satellite configuration {m, M, A_b, C, Ω; F}. Increasing values of M, C, Ω raise this limit whereas increases in m, A_b, F reduce it.

Fig. 4 shows the result of Eq. (17) for the specific Ulysses parameters. It confirms that a spin rate of 72 rpm can stabilize a slag mass of about 20 kg. If, however, the estimated value of the slag mass were to be 200 kg, a much higher spin rate of 200 rpm would be needed for stabilization.

3.4. Conditions for constant solutions

The combination of system parameters that allow constant or zero-frequency (i.e., $p=0$) solutions is of particular interest. For conservative systems they define the stability boundary, see Refs. [20,21]. For a non-conservative system, however, a root $p=0$ does *not* define the stability limit when its multiplicity equals the number of independent eigenvectors or the degeneracy of the system matrix, see Refs. [20,21]. Such a case occurred above in the subsection for $T_0=0$.

Constant solutions occur when all derivative terms in Eqs. (5a-d) vanish, so we have:

$$\begin{aligned}&(\lambda-1)\omega_2+T_{0\lambda}x_2/l=0\\&(\lambda-1)\omega_1+T_{0\lambda}x_1/l=0\\&(1-\beta_\lambda^2-T_{0\lambda})x_1-l\lambda\omega_1=0\\&(1-\beta_\lambda^2-T_{0\lambda})x_2-l\lambda\omega_2=0\end{aligned} \tag{18a – d}$$

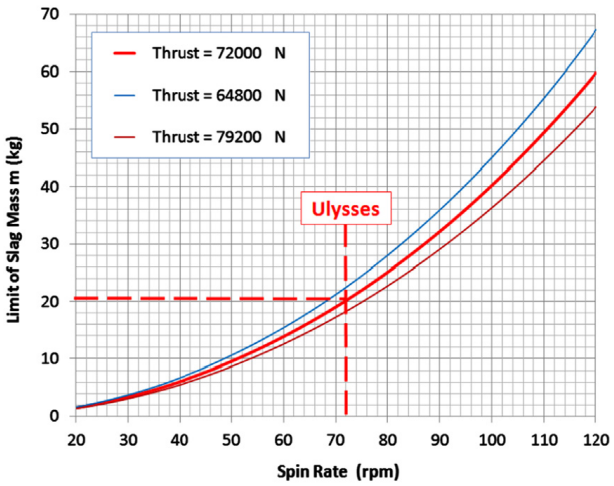

Fig. 4. Required spin rate as function of slag mass for Ulysses.

This 4×4 system decouples into two 2×2 systems in terms of the variables $\{\omega_1, x_1\}$ and $\{\omega_2, x_2\}$, respectively. The condition that the determinants of each of the 2×2 systems vanish gives the non-trivial stationary equilibrium solutions for ω_i and x_i $(i=1, 2)$. Therefore, constant equilibrium solutions exist when the following relationship between the parameters is satisfied:

$$Det\begin{bmatrix}\lambda-1 & T_{0\lambda}/l\\ -\lambda l & 1-\beta_\lambda^2-T_{0\lambda}\end{bmatrix}=0\Rightarrow T_{0\lambda}=(1-\lambda)(1-\beta_\lambda^2) \quad (19a, b)$$

The physical meaning of this result becomes more transparent when considering the original 2×2 systems in Eqs. (1). In the absence of the derivative terms, the 2×2 system $\{\omega_2, x_2\}$ is

$$(C-A_s)\omega_2+mhx_2+(\mu F/\Omega^2)x_2=0$$

$$h\omega_2-(1-\mu-\omega_{res}^2)x_2=0 \quad (20a, b)$$

The general first-order relationship between the two small attitude deviation angles $\{\theta_1, \theta_2\}$ and the non-normalized angular rate ω_2 is $\omega_2=\dot\theta_2+\Omega\theta_1$. As the normalized solution ω_2 is constant, the same is true for $\{\theta_1, \theta_2\}$ so that ω_2 equals θ_1. Making this substitution in Eq. (20a) is sufficient since Eq. (20b) will be compatible when the determinant condition is satisfied. Thus, we find a relationship between θ_1 and x_2 and similarly for θ_2 and x_1:

$$\theta_1=\frac{m(h+g/\Omega^2)}{A_s-C}x_2$$

$$\theta_2=-\frac{m(h+g/\Omega^2)}{A_s-C}x_1;\quad \text{with}: g=F/(m+M) \quad (21a-c)$$

The results of Eqs. (21) are the tilt angles of the spin axis caused by a non-zero displacement $\{x_1, x_2\}$ of the particle m and expressed in terms of the system parameters h and A_s. In the absence of the thrust, these results reduce to the standard expressions for the tilt angles due to the system cross-inertia terms $\{I_{xz}, I_{yz}\}$ induced by the non-zero particle position. The presence of the thrust force modifies these tilt angles because of the displacements x_1 and x_2.

When using the original system in Eqs. (20) we find for the determinant as in Eqs. (19):

$$\omega_{res}^2=(1-\mu)\left\{\frac{A_b-C+\mu f A_b}{A_b-C+(1-\mu)ml^2}\right\} \quad (22)$$

This result allows us to calculate the spring constant value that produces the constant tilt angles.

A mass particle on a spinning rigid body at a distance r from the spin axis feels a constant centrifugal acceleration $\Omega^2 r$ which corresponds to the state of internal stress as dictated by the rigid body model. Since our particle is not connected to any other points of the rigid body, the spring has to counteract this acceleration. Thus, in order to generate a constant solution, the effect of the spring constant k must precisely match this centrifugal force. A constant solution has always multiplicity two in the original system in Eqs. (1). This is because the tilt may occur in any direction in a symmetrical body. The remaining two roots are calculated in Appendix B.

3.5. Representation of constant solutions

The constant solutions obtained in Eq. (19b) may be visualized within the $\{T_0,\beta^2\}$ plane, while considering λ as parameter. They represent a family of straight lines $T_c(\beta^2;\lambda)$, see Fig. 5. The intersection points of the ascending and descending lines indicate that a set of system parameters that allows constant solutions may be generated by two different values of λ. The lines originate at $\beta^2=0$ with values $T_c(0;\lambda)=(1-\lambda)/\lambda^2$. They have a negative (or positive) slope for a satellite spinning about its minimum (or maximum) inertia axis, i.e., $0<\lambda<1$ (or $1<\lambda<2$).

The family of straight lines $T_c(\beta^2;\lambda)$ in Fig. 5 fills the part of the plane above their envelope curve $T_0(\beta^2)$, which is established in Appendix C as a cubic equation in $T_0(\beta^2)$:

$$T_0{}^3+(3\beta^2+1/4)T_0{}^2+(3\beta^2+5)\beta^2T_0+\beta^2(\beta^2-1)^2=0 \quad (23)$$

Every point on the envelope curve corresponds to a set of systems that allow stable stationary solutions. We show in the next section that this envelope represents also the stability boundary.

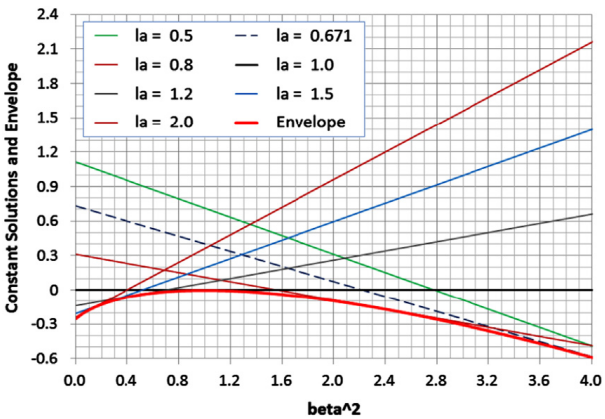

Fig. 5. Family of constant solutions $(p=0)$ and their envelope $T_0(\beta^2)$.

4. Stability results

4.1. Stability boundary

By introducing the complex variables $\omega_c=\omega_1+j\omega_2$ and $x_c=x_1+jx_2$, we can write Eqs. (5) as

$$\omega_c'-j(\lambda-1)\omega_c-jT_{0\lambda}x_c/l=0$$
$$x_c''+2jx_c'-(1-\beta_\lambda^2-T_{0\lambda})x_c+l\lambda\omega_c=0 \qquad (24a,b)$$

This complex combination of variables has a clear physical meaning. The two harmonic solutions $\{\omega_1, \omega_2\}$ have a phase shift of 90° (i.e., if ω_1 is a sine, ω_2 will be a cosine function). The same holds for $\{x_1, x_2\}$. For an asymmetric body, however, this combination is not possible.

The general case for harmonic solutions with four variables is that three of them may have an arbitrary phasing with respect to the fourth. For the system under consideration, the phases between ω_1 and ω_2 as well as between x_1 and x_2 are fixed so that only the phasing between ω_i and x_i ($i=1, 2$) is still open at this stage. An obvious advantage of using the complex combination is that the corresponding characteristic equation is of order 3 instead of 6.

To investigate the stability, it suffices to analyze the characteristic equation of Eqs. (24), while keeping in mind that each of its solutions has multiplicity two in the original system:

$$Det\begin{bmatrix} p-j(\lambda-1) & -jT_{0\lambda}/l \\ l\lambda & p^2+2jp-1+\beta_\lambda^2+T_{0\lambda}\end{bmatrix}=0 \qquad (25)$$

When introducing the frequency parameter ω defined by $p=j\omega$ we find that all three coefficients c_j ($j=1, 2, 3$) of the characteristic equation of Eqs. (25) are real:

$$\omega^3+c_2\omega^2+c_1\omega+c_0=0 \qquad (26a)$$

with:

$$c_2=3-\lambda;\quad c_1=3-2\lambda-(\beta_\lambda^2+T_{0,\lambda});\quad c_0=(1-\lambda)(1-\beta_\lambda^2)-T_{0,\lambda} \qquad (26b-d)$$

If Eqs. (26) have three *real* roots, the system is stable. The transition to one real root and two complex conjugate roots can only occur via a double root (with multiplicity four in the original system). The general condition that a cubic equation has a double root is given by Eq. (C.4) in Appendix C. When applying this condition to Eqs. (26) we obtain the following cubic equation in $T_{0\lambda}$ with coefficients that depend only on β_λ^2 and λ:

$$\tilde{S}(T_{0\lambda},\beta_\lambda^2,\lambda)=T_{0\lambda}^3+(3\beta_\lambda^2+\lambda^2/4)T_{0\lambda}^2+(3\beta_\lambda^2+5\lambda^2)\beta_\lambda^2T_{0\lambda}+\beta_\lambda^2(\beta_\lambda^2-\lambda^2)^2=0\Rightarrow$$
$$S(T_0,\beta^2)={T_0}^3+(3\beta^2+1/4){T_0}^2+(3\beta^2+5)\beta^2T_0+\beta^2(\beta^2-1)^2=0 \qquad (27a,b)$$

Obviously, the final result in Eq. (27b) is exactly identical to Eq. (23). Hence, this proves that the envelope of the stationary solutions *is* the stability curve. This property was mentioned (but not proven) in Ref. [9] in connection with the stability boundary in the presence of damping.

Fig. 6 shows the stability curve $S(T_0,\beta^2)$, which is identical to the curves shown in Refs. [7–9] for the case without damping. It is straightforward to calculate the tangent of $T_0(\beta^2)$ in Eq. (27b) from $dT_0/d(\beta^2)=-\{\partial S/\partial(\beta^2)\}/(\partial S/\partial T_0)$. This produces the slope of 45° at the origin $\beta^2=0$ and the asymptotic result of −45° for the slope at $\beta^2\to\infty$.

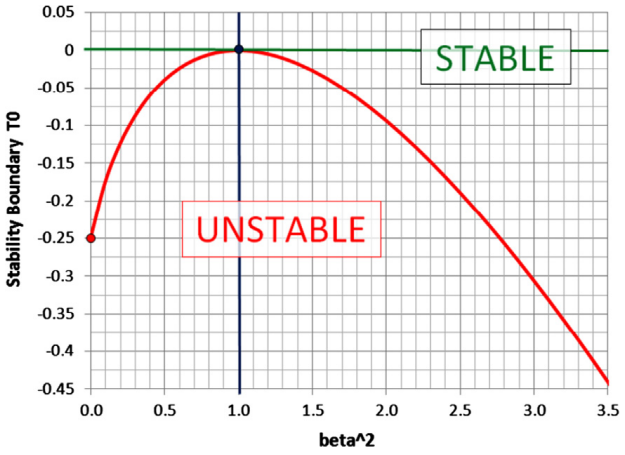

Fig. 6. Stability boundary T_0 as function of β^2 (Eq. (27b)).

After combining terms, we can write the characteristic equation in Eq. (26a) in a simpler way:

$$\omega_1^3-\lambda\omega_1^2-\lambda^2(\beta^2+T_0)\omega_1+\lambda^3\beta^2=0,\quad \text{with}: \omega_1=\omega+1 \qquad (28)$$

The new variable ω_1 is simply the frequency ω shifted by the spin rate (e.g., the zero frequency $\omega=0$ corresponds to $\omega_1=1$). The constant solutions of Eq. (28) occur when $\beta^2=0$. This is the condition that the original system has the spin rate as system frequency which agrees with Eq. (12) in the discussion for the case $k=0$ above.

An even simpler form is obtained from Eq. (28) when ω_1 is scaled by λ:

$$(\omega_1/\lambda)^3-(\omega_1/\lambda)^2-(\beta^2+T_0)(\omega_1/\lambda)+\beta^2=0 \qquad (29)$$

This equation is known as C_0 in Refs. [7–9] where it is established via changes of variables and is used for the derivation of the stability condition. The result is of course compatible with Eq. (27b) which follows directly from the characteristic equation of the system in Eqs. (24).

It is of interest to note that Ref. [10] produces a similar stability curve for the case when the internal motion is due to a spherical pendulum. In this case, the frequency ω_{res}^2 contained in the horizontal coordinate β^2 is simply replaced by the normalized pendulum frequency (i.e., $g/(\Omega^2|l|)$ or F_r^{-1} in the notations of Ref. [10]). For the vertical coordinate T_0, the pendulum attachment location z_0 replaces l in the p_{th} and p_k parameters which contain now also the particle mass. This observation illustrates how the parameter k may be linked to alternative models for internal motion.

4.2. Representations of stability boundary in k_n and μ

Next, we express the stability curve in the physical parameters k_n and μ. By using the parameters p_{th}, p_{res}, and p_k (see Table 2), we can replace $T_{0\lambda}$, β_λ^2 in Eq. (27a) by:

$$\beta_\lambda^2=k_n\,p_{res}/\mu=ak_n;\quad T_{0\lambda}=k_n-\mu f=k_n-b \qquad (30a,b)$$

with : $a = p_{res}/\mu; \quad b = \mu f$ (30c − d)

Because both substitutions in Eqs. (30a,b) are linear in k_n, we obtain a cubic equation in k_n with coefficients d_i that depend on the parameters a and b, defined in Eqs. (30c,d), and λ:

$$\widehat{S}(k_n) = k_n^3 + d_2 k_n^2 + d_1 k_n + d_0 = 0 \quad (31a)$$

with:

$$d_2 : -3b/(1+a) + \lambda^2\{1/4 + 5a - 2a^2\}/(1+a)^3$$

$$d_1 : 3b^2/(1+a)^2 + \lambda^2\{a\lambda^2 - b/2 - 5ab\}/(1+a)^3$$

$$d_0 : b^2(\lambda^2/4 - b)/(1+a)^3 \quad (32a - c)$$

Because k_n is the normalized spring constant, the only physically meaningful roots of the cubic polynomial in Eq. (31a) are those that are real and positive. Table 4 provides a summary of the signs of the three roots for k_n for different ranges of the slag mass ratio μ for the Ulysses data.

Table 4 shows that root 1 is always real and positive. Its behavior as a function of β^2 is illustrated in Fig. 7a for the part of the curve that is of interest in practice, i.e. $\mu < 0.133$ corresponding to $m = 90$ kg. After substituting root 1 back into Eqs. (30) and using Eqs. (27) we reestablish the corresponding curve in the $\{T_{0\lambda}, \beta_\lambda^2\}$ plane, see Fig. 7b. It starts with mass ratio $\mu = 0$ at point A, i.e. $\{\beta_\lambda^2 = \lambda^2 = 0.450, T_{0\lambda} = 0\}$ which corresponds to the point $\{\beta^2 = 1, T_0 = 0\}$ in Fig. 6. At the mass ratio of $\mu = 0.133$, the k_n value has increased to 0.359 and β_λ^2 to 1.15 which corresponds to $\beta^2 = 2.56$ in Fig. 6. Figs. 7b and 6 show that, at least in the half-plane $\beta_\lambda^2 > \lambda^2$ (or $\beta^2 > 1$), an increase in the spring stiffness k has always a positive effect on the stability.

Table 4 shows that root 2 is the only other root that produces a positive k_n and this only in a limited range of the mass ratio. As shown in Fig. 7c, $k_n > 0$ in the range from point C to point D where $\mu \approx 0.0333$ (i.e., $m \approx 20.2$ kg). Fig. 7d shows that the part of the stability curve corresponding to root 2 covers the range $0 < \beta_\lambda^2 < 0.45$ (i.e., $0 < \beta^2 < 1$ in Fig. 6). The origin $\mu = 0$ of Fig. 7c corresponds to point C, which is $\{\beta_\lambda^2 = \lambda^2, T_0 = 0\}$ in Fig. 7d and {1,0} in Fig. 6.

The point C in Fig. 7d matches precisely with point A in Fig. 7b. When μ increases, so does k_n initially, see Fig. 7c. At point E, for $\mu = 0.0127$, k_n reaches its maximum value of 4.08×10^{-3} or $k = 58.5$ kg/s^2 and then returns to zero at point D with mass ratio 0.0333. The end-point D on the $T_{0\lambda}$ axis in Fig. 7d is $T_{0\lambda} = -\lambda^2/4 = -0.1125$ or $T_0 = -1/4$, which is consistent with the result in Eq. (15a). When combining Fig. 7b and d (and scaling by the constant λ^2), we retrieve Fig. 6.

Fig. 6 shows that the point $\{T_0 = 0, \beta^2 = 1\}$ represents the worst case for stability. In Fig. 7c and d this point corresponds to point C where $m = k = 0$. It is a singular case since there is no particle but only the rigid body. The k value is meaningless when m vanishes as there is no mass on which the spring may act. When approaching point C *along the boundary curve*, k and m go to zero at the same rate so that ω_{res}^2 (and β^2) have finite limits. In other words, when the resonance frequency of the spring-mass system approaches the body's precession frequency $\lambda = C/A_b$, the mass m of the particle that can be stabilised goes to zero (i.e., $m \to 0$, $\mu \to 0$, and $\beta^2 \to 1$).

The properties of the stability boundary for β_λ^2 over the interval $(0, \lambda^2 = 0.45)$ in Fig. 7c and d are surprising. Starting from point D (i.e., $\beta^2 = k = 0$), Fig. 7c shows that an increase in k_n *reduces* the slag mass that can be stabilized and continues to do so until the particle mass ratio reaches the value 0.0127 at point E. Afterwards, while staying on the boundary curve, k and m decrease to zero. Finally, at point C, both the k_n and μf terms of T_0 vanish separately but ω_{res}^2 remains well-defined as was mentioned in the previous paragraph.

Fig. 8 illustrates the evolution of the resonance frequency $\omega_{res}^2 = (1-\mu)\beta_\lambda^2$ of the spring *on the stability boundary* as function of the particle mass that can be stabilised. Starting from point D, i.e. $k_n = 0$, $m = 0.0345$ M (or $\mu = 0.0333$), the resonance frequency increases to the value $\lambda^2 = 0.450$ at point A=C when the particle mass approaches zero on the lower (blue) curve. Subsequently, the frequency follows the upper (red) curve and increases again until its maximum value at point B with mass ratio $\mu = 0.133$ in Fig. 7a. The maximum is reached at point B in Fig. 8 with $m/M = 0.153$ (i.e., $m = 90$ kg), which corresponds to $\beta_\lambda^2 = 1.15$ or $\beta^2 = 2.56$. The decrease of the resonance frequency to the right of point B proves that the increase of β^2 in Fig. 6 for values beyond $\beta^2 = 2.56$ is due to an increasing slag mass and not because of an increasing value of ω_{res}^2.

Table 4
Spring constant k_n versus slag mass ratio μ (Ulysses values).

Slag mass ratio μ	**Spring constant** k_n		
Interval	Root 1	Root 2	Root 3
0–0.03334	> 0	> 0	< 0
0.03334–0.03906	> 0	< 0	< 0
> 0.03906	> 0	Complex conjugate	

4.3. Different representations of the stability boundary

The properties of the boundary curves can be more easily understood by studying the mapping from $\{T_{0\lambda}, \beta_\lambda^2\}$ onto $\{k_n, \mu\}$ in more detail. The definitions in Table 2 suggest that it is straightforward to parameterize the relationship $T_{0\lambda}(\beta_\lambda^2)$ in either k_n or μ:

$$T_{0\lambda}(\beta_\lambda^2; k_n) = k_n(1 - f\, p_{res}/\beta_\lambda^2); \quad T_{0\lambda}(\beta_\lambda^2; \mu) = \mu(\beta_\lambda^2/p_{res} - f) \quad (33a, b)$$

Eq. (33a) defines a family of hyperbolas based on the parameter k_n and Eq. (33b) identifies a family of straight lines based on μ, respectively. Thus, we can plot loci of constant k_n and μ (which are both positive) as illustrated in Fig. 9a–d where each combination $\{k_n, \mu\}$ corresponds to a point in the $\{T_{0\lambda}, \beta_\lambda^2\}$ plane. For the case $l > 0$, Fig. 9a shows that all feasible points lie within the first quadrant of the $\{T_{0\lambda}, \beta_\lambda^2\}$ plane and, therefore, represent stable configurations.

The case $l < 0$ in Fig. 9b–d is more complicated. When using the Ulysses data and starting on the $T_{0\lambda}$ axis we find from Fig. 9c and d that the mass ratio $\mu \approx 0.0333$ ($m \approx 20.2$ kg) is the maximum that can be stabilised without the spring. When moving along the line for this mass ratio (and adding the spring), we enter immediately into the

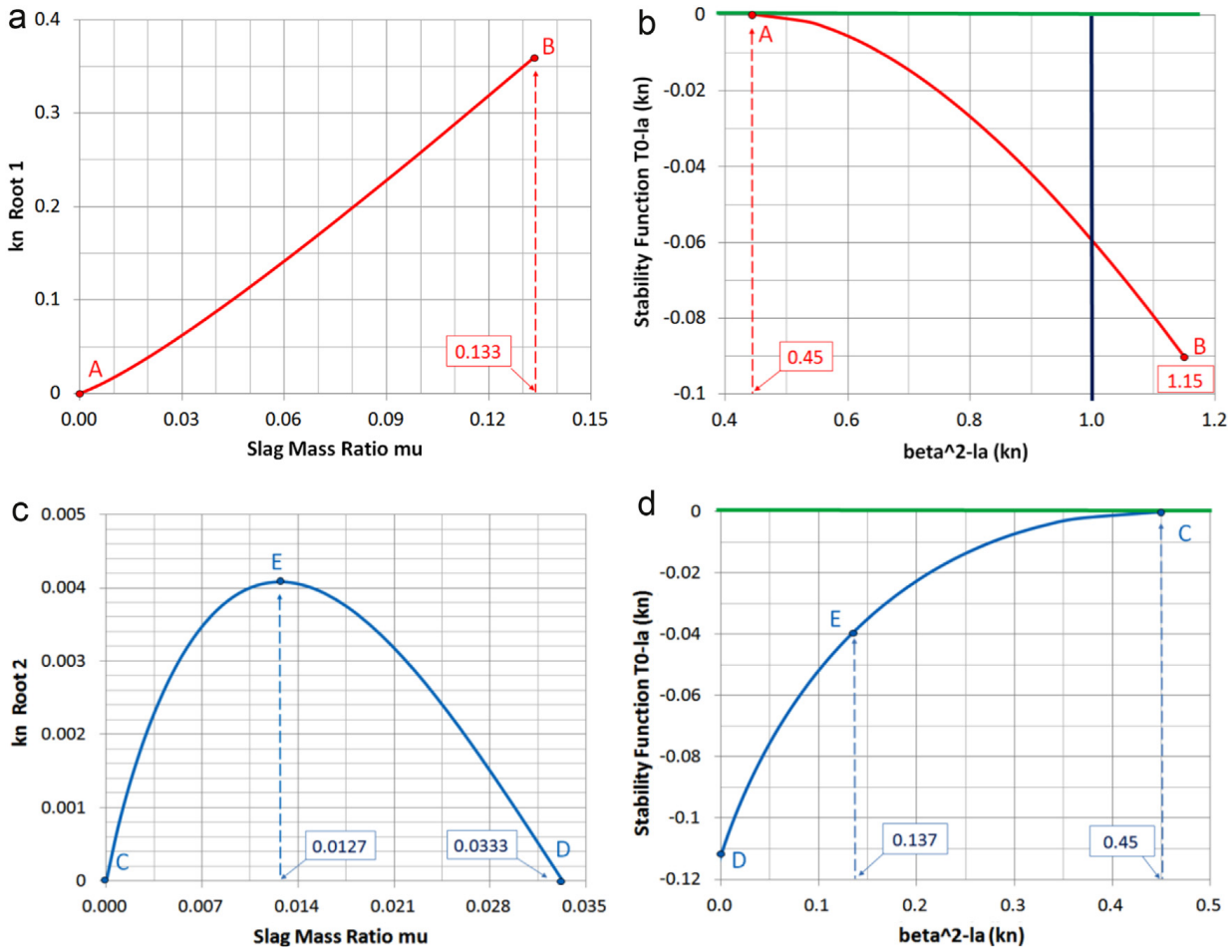

Fig. 7. (a) $k_n(\mu)$ for Root 1, (b) k_n for Root 1 in $\{\beta_\lambda^2, T_{0\lambda}\}$ plane, (c) $k_n(\mu)$ for Root 2 and (d) k_n for Root 2 in $\{\beta_\lambda^2, T_{0\lambda}\}$ plane.

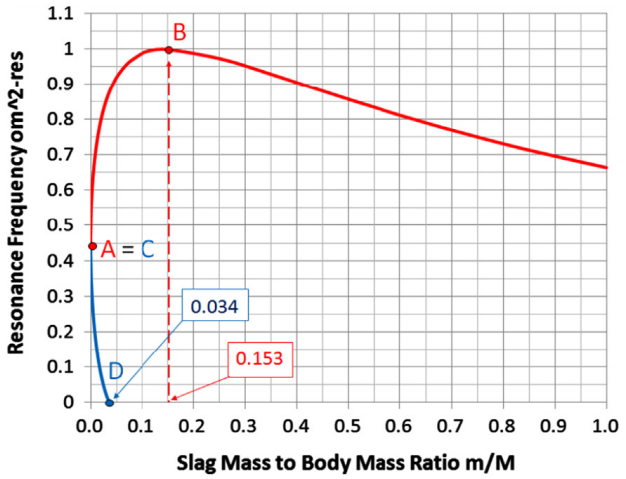

Fig. 8. ω_{res}^2 versus slag mass/body mass on stability boundary. (For interpretation of the references to color in this figure legend, the reader is referred to the web version of this article.)

unstable domain. For increasing k_n, the system becomes stable when $k_n=0.07$, i.e. at $\beta_\lambda^2=0.9$ or $\beta^2=2.0$, see Fig. 9c and d. The same applies when starting from an unstable system and a higher mass ratio. However, when starting from a stable system with a smaller mass ratio, we enter the unstable domain for some small k_n value and exit when the stiffness has increased significantly. Thus, for smaller mass ratios, there is a range of stiffness values that destabilize the system. This range approaches zero together with the mass ratio (note that the system is stable for $\mu=0$). Fig. 9b shows that the hyperbolas for small k_n values cut the stability boundary twice which confirms the discussion of Fig. 7c. The point E of Fig. 7c lies on the curve ($k_n=0.0042$, $\mu=0.0127$) in Fig. 9c where it touches the stability boundary on its convex side. Higher k_n values stay below the boundary and lower k_n cut the boundary twice.

A significant part of the second quadrant of the $\{T_{0\lambda}, \beta_\lambda^2\}$ plane corresponds to unrealistic slag masses. The point $\beta_\lambda^2=fp_{res}=1.4395$ or $(\beta^2)_{max}=fp_{res}/\lambda^2=3.1986$ is the maximum that needs to be considered, regardless of the k and m values. This is because, when assuming positive k values, we find that values of $\beta^2>3.1986$ correspond to values $T_0>0$ which are in the *first* quadrant.

4.4. Consequences for double roots

The limit on the permissible value for β_λ^2 has consequences for the possible values of the double root. When the condition for a double root ω_d is met, this root is also a solution of the derivative of the characteristic equation.

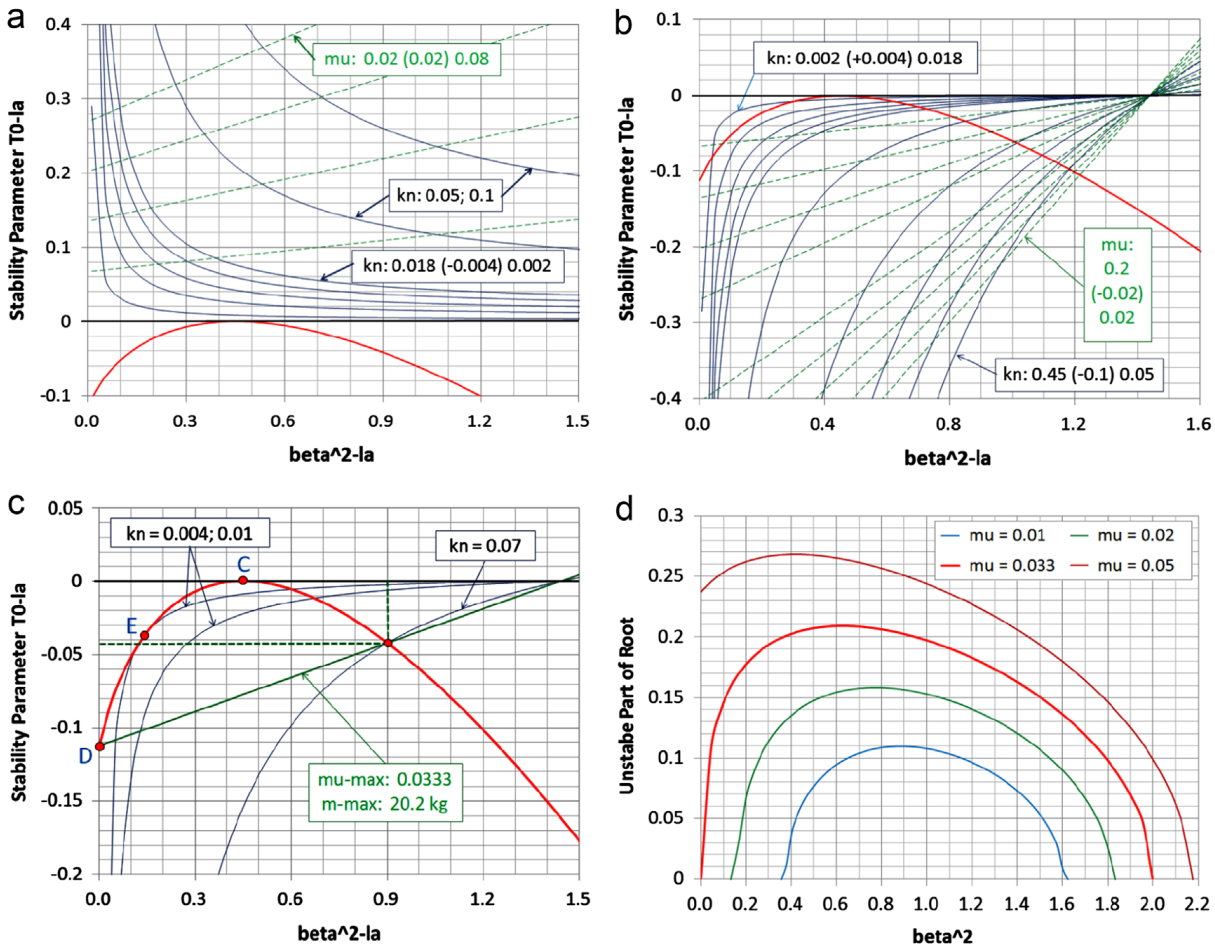

Fig. 9. (a) parametric lines in k_n, μ for $l=1.5$; (b) parametric lines in k_n, μ for $l=-1.5$; (c) stability limit for Ulysses case and (d) extent of instability for μ values.

For instance, in the form of Eq. (28) we have:

$$3\omega_{1d}^2-2\lambda\omega_{1d}-\lambda^2(\beta^2+T_0)=0 \tag{34}$$

Therefore, the loci of double roots are given by the straight lines $T_d(\beta^2;\lambda)$ as follows:

$$T_d=-\beta^2+(3\omega_{1d}/\lambda-2)\omega_{1d}/\lambda \tag{35}$$

where ω_{1d} is one of the roots of Eq. (34). These lines are illustrated in Fig. 10 and their intersections with the stability boundary provide the values of the double roots. Any line parallel to the second bisector must cut the stability curve because its asymptotic direction for $\beta^2\to\infty$ is -45°.

The coordinate of the end-point T_e of these lines on the T_0 axis is found as

$$T_e=T_d(\beta^2=0)=3(\omega_{1d}/\lambda)^2-2\omega_{1d}/\lambda \tag{36}$$

This parabola in (ω_{1d}/λ) reaches its top at the coordinates $\{T_e=-1/3,\ \omega_{1d}/\lambda=1/3\}$ but the corresponding line $T_d=-(\beta^2+1/3)$ does not intersect the stability curve. Fig. 10 shows that the minimum value of T_e is $-1/4$ as was calculated in Eq. (15a). This corresponds to the values $\omega_{1d}/\lambda=1/2$, $1/6$ and $\omega_d=\lambda/2-1$ and $\lambda/6-1$. The first solution belongs to the plus sign and is the result of Eq. (14b) whereas the other one is an extreme value of the characteristic equation in Eq. (34). When the end-point $T_e=0$ we find $\omega_{1d}/\lambda=2/3$ which corresponds to $\omega_d=2\lambda/3-1$.

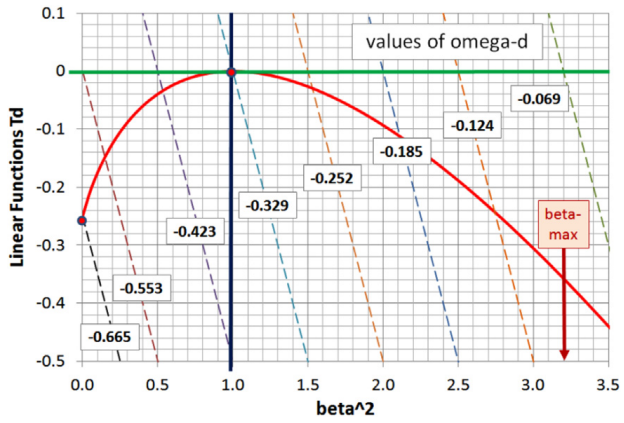

Fig. 10. Lines defining the possible values of the double root.

The line with end-point $T_e=1$ intersects the stability curve at $\beta^2=1$ and gives $\omega_d=\lambda-1$ which corresponds to the nutation motion in Eq. (8a) and agrees with all statements regarding the point $\beta^2=1$. The end-point $T_e=2$ produces the root $\omega_{1d}=(1+\sqrt{7})\lambda/3\approx 1.215\lambda$ and $\omega_d=\omega_{1d}-1$. The intersection of the stability curve occurs when $\beta^2\approx 2.1$ which is getting closer to its maximum possible value. Finally, Fig. 10 indicates that the end-point $T_d=3$ leads to an intersection of the stability boundary at $\beta^2\approx 3.4$. This is beyond the value of $(\beta^2)_{max}=3.1986$ so this result is not meaningful. Finally, we mention that the

analysis of the possible range for ω_d may also have repercussions on the validity of the stability boundary derived in Ref. [9] for the case with damping.

5. Conclusion

The paper analyzes the instability caused by the STAR-48 solid rocket motor on the basis of the model proposed in the pioneering paper by Mingori and Yam [7]. Their model considers a mass particle attached via a spring to the satellite body to describe the internal motion of the slag mass within the motor. The present study reformulates the stability condition in terms of the two parameters that represent the internal motion and are directly responsible for the stability. This different approach leads to valuable new insights in the stability characteristics. An analytic form of the stability boundary is established and it is proven that this boundary is identical to the envelope of the stationary (i.e., constant) equilibrium solutions. This is an interesting theoretical result as it connects the existence of a stationary solution of a non-conservative system to its stability. The relation between the manifold defining the stability boundary and the physical parameters shows that only part of this manifold corresponds to a physical system. The case of most practical interest is when the slag mass is aft of the body's center of mass. The system is unstable when the spring is absent and the particle mass exceeds a given value. It may then be stabilized by adding a spring of sufficient stiffness which is intuitively clear. For a sufficiently small slag mass, the system is stable even in the absence of the spring. When increasing the spring stiffness in this case there will be a value for which the system becomes unstable. A further increase of the stiffness will stabilize the system again. The range of the stiffness values that destabilize the system in this case shrinks and approaches zero along with a decreasing slag mass. The paper also provides explicit results for the values of the double roots located on the stability boundary.

Appendix A. MGKN formulation

After introducing the small attitude angles $\{\theta_1, \theta_2\}$ we can eliminate $\{\omega_1,\omega_2\}$ from Eq. (1) by substituting:

$$\omega_1 = \dot{\theta}_1 - \Omega\theta_2; \quad \omega_2 = \dot{\theta}_2 + \Omega\theta_1 \tag{A.1}$$

The state vector $q^T=[\theta_1, \theta_2, x_1, x_2]$ describes small deviations from the reference state $q=0$ in a frame rotating uniformly at Ω (which is not a body-fixed frame). By using the 'Ansatz' $exp(p\tau)$, we can write the equations in matrix form as $Z(p)q=0$ where $Z(p)$ stands for the matrix:

$$Z(p)=\begin{bmatrix} A_s p^2-(A_s-C) & -(2A_s-C)p & -2mh\,p & -mh(p^2-1)+\mu F/\Omega^2 \\ (2A_s-C)p & A_s p^2+(A_s-C) & mh(p^2-1)-\mu F/\Omega^2 & -2mhp \\ 2mhp & mh(p^2-1) & m\{\omega_{res}^2+\mu_1(p^2-1)\} & -2m\mu_1 p \\ -mh(p^2-1) & 2mhp & 2m\mu_1 p & m\{\omega_{res}^2+\mu_1(p^2-1)\} \end{bmatrix} \Rightarrow Z = Mp^2+Gp+(K+N) \tag{A.2a, b}$$

with $\mu_1=1-\mu$, $M=M^T=0$, $K=K^T$, $G=-G^T$, and $N=-N^T$.

We note that M is the mass matrix and that the anti-symmetric matrices G and N are typical for a spinning system with follower forces. The thrust F changes the generic model from a conservative MGK system to a non-conservative MGKN system which has a profound impact on the possible instability mechanisms (see Refs. [20,21]). In the case of an MGK system, the transition from stability to instability always implies that a system frequency, as function of a parameter, has reached zero. For an MGKN system, when two system frequencies have approached each other and become equal at a non-zero value, they may leave the imaginary axis and go in opposite directions on the real axis which is known as a flutter type of instability.

Appendix B. Remaining roots when stationary solutions exist

The condition for constant solutions $\omega=0$ in Eq. (26a) is $c_0=0$, which agrees, of course, with Eq. (19b). In this case, the two other roots are the solutions of the remaining quadratic equation:

$$\omega^2+c_2\omega+c_1=0 \Rightarrow \omega_{1,2}=-(3-\lambda)/2 \pm \sqrt{(\lambda-1)^2/4+\lambda^3\beta^2} \tag{B.1}$$

The roots $\omega_{1,2}$ are *real* and are different from each other for any values $\{\lambda,\mu,\omega_{res}^2\}$, see Fig. 11. Therefore, in the present model without damping, the system is stable if stationary solutions exist.

Appendix C. Envelope of polynomial curves

Here we provide a summary of the formulae needed to compute the envelope of an implicit function $F(T_0,\beta^2)$ that depends also on a parameter λ as applied to Eq. (19b) and shown in Fig. 5:

$$F(T_0,\beta^2;\lambda)=T_0+(1-\lambda)(\beta^2-1/\lambda^2)=0 \tag{C.1}$$

In general, the envelope of a function F is given by the condition:

$$F-\frac{\partial F}{\partial \lambda}=0 \tag{C.2}$$

When F is a rational function of λ, we obtain the polynomial F_c after clearing the fractions:

$$F_c(T_0,\beta^2;\lambda)=T_0\lambda^2+(1-\lambda)(\lambda^2\beta^2-1)=0 \tag{C.3}$$

The envelope is then given by the requirement that λ is a double root of F_c.[2] In this case, F_c is a cubic polynomial of the form $a\lambda^3+b\lambda^2+c\lambda+d=0$ and the condition for a double root[3] is

$$b^2c^2-4ac^3-4db^3-27a^2d^2+18abcd=0 \tag{C.4}$$

[2] http://en.wikipedia.org/wiki/Envelope_(mathematics).

[3] This condition is better known for $a=1$; after elimination of the quadratic term $b=0$ we have $(c/3)^3+(d/2)^2=0$.

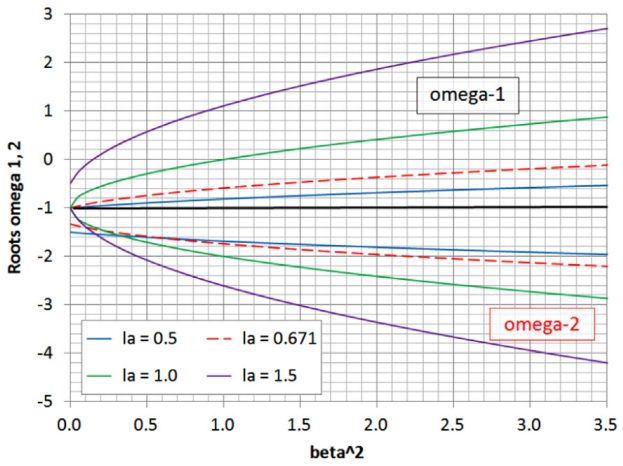

Fig. 11. Roots ω_1, ω_2 for $0.5<\lambda<1.5$ when constant solutions exist.

with $a=-\beta^2$; $b=T_0+\beta^2$; $c=1$; $d=-1$. This leads to the following cubic polynomial in T_0:

$$T_0{}^3+(3\beta^2+1/4)T_0{}^2+(3\beta^2+5)\beta^2T_0+\beta^2(\beta^2-1)^2=0 \quad \text{(C.5)}$$

References

[1] G.A. Flandro, et al., Fluid Mechanics of Spinning Rockets, Report AFRPL TR-86-072, Fluid Dynamics Laboratory, Air Force Rocket Propulsion Laboratory, Edwards AFB (CA), January 1987.

[2] D. Javorsek II, J.M. Longuski, Velocity pointing errors associated with spinning thrusting spacecraft, J. Spacecr. Rockets 37 (3) (2000) 359–365.

[3] R.X. Meyer, Convective instability in solid propellant motors, Adv. Astronaut. Sci. 54 (1983) 657–669.

[4] D.L. Misterek, J.W. Murdock, S. Koshigoe, Gas-dynamic flow in a spinning, coning solid rocket motor, J. Propul. Power 9 (1) (1993) 35–42.

[5] F.L. Janssens, Jet damping and nutation growth during the burn of a solid rocket motor such as PAM-D, ESA J. 12 (3) (1988) 273–288.

[6] R.X. Meyer, Coning instability of spacecraft during periods of thrust, J. Guidance, Control Dyn. 33 (6) (1996) 781–788.

[7] D.L. Mingori, Y. Yam, Nutational stability of a spinning spacecraft with internal mass motion and axial thrust, in: Proceedings of the AIAA/AAS Astrodynamics Conference. Williamsburg, VA, August 1986, Paper AIAA-1986-2271.

[8] D.M. Halsmer, D.L. Mingori, Nutational stability and passive control of spinning rockets with internal mass motion, J. Guidance, Control Dyn. 18 (5) (1995) 1197–1203.

[9] Y. Yam, D.L. Mingori, D.M. Halsmer, Stability of a spinning axisymmetric rocket with dissipative internal mass motion, J. Guidance, Control Dyn. 20 (2) (1997) 306–312.

[10] A.C. Or, Rotor-pendulum model for the perigee assist module nutation anomaly, J. Guidance, Control Dyn. 15 (2) (1992) 297–303.

[11] A.C. Or, A.D Challoner, Stability of spinning spacecraft containing shallow pool of liquid under thrust, J. Guidance, Control Dyn. 17 (5) (1994) 1019–1027.

[12] J.E. Cochran, J.Y. Kang, Nonlinear stability analysis of the attitude motion of a spin-stabilised upper stage, Adv. Astronaut. Sci., Spaceflight Mech. 75 (1991) 345–364.

[13] J.Y. Kang, J.E. Cochran, Resonant motion of a spin-stabilised thrusting spacecraft, J. Guidance, Control Dyn. 27 (3) (2004) 356–364.

[14] J.Y. Kang, J.E. Cochran, Stability criteria of slosh motion with periodicity in a spinning spacecraft, J. Guidance, Control Dyn. 28 (3) (2005) 562–567.

[15] R.X. Meyer, In-flight formation of slag in spinning solid propellant rocket motors, J. Propul. Power 8 (1) (1992) 45–50.

[16] J. Dupays, Y. Fabignon, O. Orlandi, J.-F. Trubert, Combustion of aluminium particles in solid rocket motors, in: Proceedings of the 2nd ONERA/DLR Aerospace Symposium, June 15–16, Berlin, Germany, 2000, Paper ONERA TP 2001-8.

[17] E.B. Crellin, Investigation of Nutational Instability for Ulysses and PAM-S, Working Paper 1522, ESA/ESTEC, August 1988.

[18] F.L. Janssens, Stability of a Spinning Rigid Body with Axial Thrusting and Moving Internal Mass Report ISPM-RE-7284, ESA/ESTEC, April 1989.

[19] J.C. van der Ha, F.L. Janssens, Jet damping and misalignment effects during solid-rocket-motor burn, J. Guidance, Control Dyn. 28 (3) (2005) 412–420.

[20] P.C. Müller, Stabilität und Matrizen, Spinger Engineering Science Library, Berlin, Germany, 1977.

[21] P.C. Hughes, Spacecraft Attitude Dynamics, Dover Publications, Mineola, NY, 2004Dover Publications, Mineola, NY, 1986 (first edition, John Wiley & Sons, New York, NY).

[22] F.L. Janssens, J.C. van der Ha, On the stability of spinning satellites, Acta Astronaut. 68 (7–8) (2011) 778–789.